Comparative numerical study of rate-dependent continuum-based plasticity models for high-velocity impacts of copper particles against a substrate

Giedrius Jočbalis [a,*], Rimantas Kačianauskas [b], Sergėjus Borodinas [b], Jerzy Rojek [c]

[a] *Antanas Gustaitis Aviation Institute, Vilnius Gediminas Technical University, Vilnius, Lithuania*
[b] *Department of Applied Mechanics, Vilnius Gediminas Technical University, Vilnius, Lithuania*
[c] *Institute of Fundamental Technological Research, Polish Academy of Sciences, Warsaw, Poland*

ABSTRACT

The problem of high-rate elastic-plastic deformation of micro-sized copper particles impacting against a copper substrate was investigated by applying the continuum-based formulation and finite element thermomechanical analysis. Comparative study of selected plasticity models was performed. The aim of the paper was to study strain rate-dependant plasticity for a wide range of strain rates. The strain-rate-dependant Johnson-Cook and Cowper-Symonds models were studied by comparing displacements, velocities, strains, strain rates, stresses, contact forces, and temperatures and their contribution to material yield stress. The study shows the importance of the high-strain rate yielding model and its adequacy for experimental data. Both models complement each other and may be regarded as soft and hard bounds of the solution. A new, combined, two-function model, containing two independent functions for each of the two ranges, is suggested. The proposed model describes a low strain rate sensitivity range using the Johnson-Cook expression, while allows fitting of the model for experimental results in a high strain rate sensitivity range, using a modified Cowper-Symonds expression. This combination is capable of describing both low and high strain rate regimes, giving the minimum deviation from experimental results.

1. Introduction

The evaluation of plastic contact deformation of a particle colliding with a specified target surface is a topic of major interest in a broad variety of fundamental studies and industrial applications. Advanced technology aimed at producing 3D shapes by joining the smallest parts of materials is commonly referred to as additive manufacturing (AM). One particular case of AM technology is particle spraying, in which one material is coated with different another material using high-velocity particle-substrate interaction. Although a large number of results, covering various aspects of spray technology, have been published, we restrict ourselves to referring to a limited number of reviews, redirecting the reader to the references herein. The scientific aspects and recent developments of the particular case of cold spray (CS) technology may be found in the review papers by Moridi et al. [1] and Dowding et al. [2]. Warm spray technology is described in the papers of Kuroda et al. [3] and Oviedo et al. [4].

The majority of AM technologies, especially particle spray, operate with a large number of particles interacting with each other. Simulation of a multiparticle system is performed by considering binary contacts; therefore, the evaluation of the single isolated particle impact is important for many reasons. Disregarding specific properties of particular technologies, we concentrate on the simulation of the single impact of a particle on the substrate in the normal direction. The impact process is considered as an isolated binary collision of 3D solid bodies. Here, the detailed description of the contact zone is the major priority. Consequently, using continuum-based approach is a natural way to consider the interaction.

The collision of particles is a time-dependant process, which is formulated in terms of continuum variables defined in the volume of colliding homogeneous bodies. The problem is described by coupled thermal and mechanical state equations. Here, the constitutive relations are predefined in an incremental form, while the yielding is defined by yield criteria. For metallic materials, von Misses' plasticity criterion is used. Plastic hardening (softening) law is predefined by phenomenological yield stress function, known as the plasticity model. It is obvious that the plasticity model reflects material properties, while the co-efficients of the model need to be validated by experimental data.

The classical continuum-based strain hardening plasticity models are quasistatic. Historically, probably the earliest suggestion to describe

---

strain hardening by a power-law approximation of the experimental stress-strain curve was made by Ludwik [5]. This model describes the initial yield strength and its increase due to the plastic strain. The Hollomon model [6] assumes that the material has no initial yield strength. Meanwhile, in the Swift model [7], the initial yield strength is expressed through the initial strain. The Voce model [8] describes strain dependency exponentially, while also limiting yield strength with saturation value. These models are relevant to low-speed impact and static loading. The state of the art in the modelling of plastic contacts in a wide variety of geometry, plasticity models, and loading situations is summarised in the review by Ghaednia et al. [9].

The low-speed impact is probably used the most and understood the best. The demand for a low-speed particle impact solution increased strongly with the development of the discrete (distinct) element method (DEM), introduced by Cundall and Strack [10]. Here, the elastic particle contact between spherical surfaces was solved by Hertz theory [11], and an analytical solution was obtained. A local solution of the contact problem is defined as a three-dimensional variation of stresses and strains. It may be transformed into a macroscopic particle force and displacement relationship and then further applied in multiparticle systems.

The Hertz analytical solution was later extended concerning the propagation of plastic deformation. Various nonlinear elastic-plastic contact models applicable in DEM were proposed by Thornton [12], Zhang and Vu-Quoc [13], Weir and Tallon [14], and Rojek et al. [15]. The importance of accounting for strain rate sensitivity, even at low impact velocities, was shown by Minamoto et al. [16].

The increase of impact velocity and the reduction of particle size towards micro-scale leads to significant complications, due to which, the impact of a high-velocity micro-particle on a substrate is characterised by an extremely high plastic strain rate and high temperature. The plasticity model incorporates multiplicative strain, strain rate and temperature functions, allowing different plasticity model combinations. A review of selected plasticity models is given in the work of Hor et al., 2013 [17].

Contact velocities in spray technologies vary from 300 and may reach up to 1200 m/s [18]. The strain rates in a cold spray can easily reach ranges of 10^{10} s^{-1} [19]. Additional yielding mechanisms, related to the strain rates and temperature, have to be taken into account.

Classical plasticity models can accurately describe a limited range of strain rate; therefore, they are used to simulate different processes, undergoing a limited range of strain rates. One of the most popular models is the logarithmic Johnson-Cook (J-C) model [20]. Other, simpler, forms of logarithmic models were described by Ludwik [5] and Sokolovskii [21]. The higher gradient of a strain rate can be described by the Cowper-Symonds (C-S) model [22] using the power law.

More complex models like Huh-Kang [23] used a more elaborate logarithmic form, while the Tuazon model [24] used a combination of the logarithm and power law. A different combination of logarithmic and power law models to define strain rate sensitivity more accurately was used in the Couque model [25]. Meanwhile, the Yu et al. model [26] divides strain rate sensitivity into three regimes assuming that strain rate hardening reaches the saturation value. A conceptual comparison of various rate-dependant models is shown in Fig. 1.

The dependence of the yield stress on the temperature at higher strain rates can be adequately described using simple models. For example, the Litonsky law and the Zhao and Gary [27] models describe the dependency as linear, whereas the Vinh et al. [28] model dependency is exponential. Meanwhile, the Johnson-Cook thermal softening model [20] uses approximation by power law.

An important stage of modelling is computer implementation and application of suitable software codes. Continuum-based models are almost routinely formulated by the finite element method and implemented into the finite element code. Modelling of the process allows evaluation of microscopic parameters within the particle, which is otherwise difficult to obtain experimentally. The full solution of the elastic-plastic thermomechanical high-velocity impact problem comprises the evaluation of stresses and strains, strain rates, temperatures, etc., as well as particle displacements and particle-substrate interaction forces.

Since the plastic zone is initially smaller than the particle size, the solution domain discretized by FEM using refined mesh [29]. Various simulations of a CS process, involving particle-to-substrate collision, were performed by many authors. A simpler approach, accounting only for thermal softening, was simulated by Schmidt et al. [30]. Most other simulations were performed using the J-C strain rate plasticity model (for example Yokoyama et al. [31], Mebdoua et al. [32], additionally the impact of a particle coming into contact at an angle, Li et al. [33]). Razavipour and Jodoin [34] compared impact simulation results using the Preston-Tonks-Wallace and J-C models. Impact simulations using the C-S model were performed by Petkevič et al. [35]. A bilinear strain rate hardening description of an aluminium particle using the J-C model was applied by Xie et al. [36]. Similar high-velocity impact problems solved with DEM include shot peening [37] and high-velocity compaction [38].

The previously described continuum-based models are limited to homogenous material. Therefore, they do not reflect the microstructure of the material. Dislocations theory is used to describe underlying mechanisms of high-rate plasticity on a micro level. The discrete concept of dislocations may be found in the works of [39,40,41,42]. These models are characterized by the maximum strain-rate limit due to maximum dislocation velocity defined by dislocation density. The influence of dislocations is mostly observed in metallurgy when
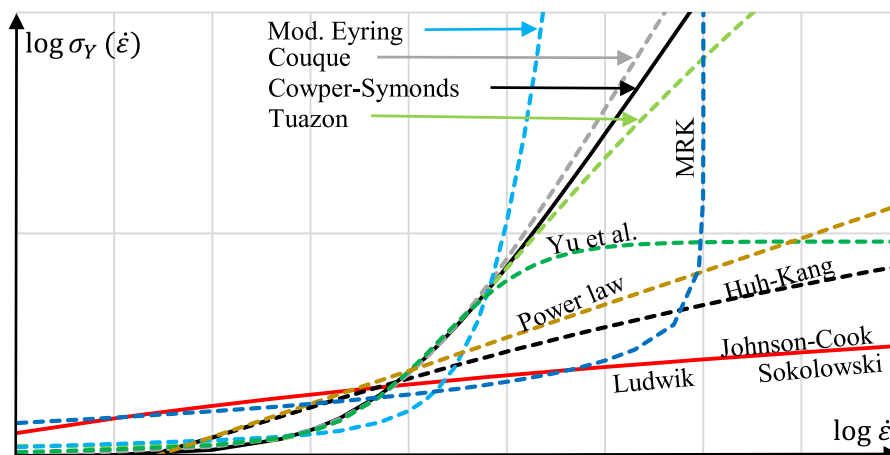

Fig 1. Illustration of strain-rate hardening models in yield strength – strain rate plane.

investigating single crystal plasticity. Modelling material behaviour on a microscale requires new computational approaches. Here, molecular dynamics and discrete dislocation dynamics may be applied. The application of these methods in particle mechanics requires new types of the numerical approach. The microphysics could be better evaluated by using dislocation-based plasticity models that aim to describe strain rate hardening based on dislocations of material crystal structure. For example, the exponential Eyring model was modified by Al Salahi and Othman [43], or modified Rusinek-Klepaczko model [44]. However, these models are difficult to implement in high-velocity particle impact simulations due to the initial impact strain rate exceeding the strain rate limit of the model. The dislocation-based characterisation of high-rate material properties of high-purity copper at elevated temperatures was reviewed by Lea and Jardine [40], and Almasri and Voyiadjis [45].

Based on the review above, it was observed that recent theoretical research concentrates on the development of the common framework for evaluation and application of plasticity behaviour, in describing contact at high impact velocities, as well as evaluation of high strain rate material parameters. The most important high strain rate plasticity characteristic includes describing the variation of yield stress parameter against the entire range of strain rates. Experimentally obtained yield stress is characterised by a bilinear relationship [46]. The adequacy of plasticity models to a numerically simulated process with a wide range of strain rates, including threshold value, must be observed. Therefore, evaluation by a single constant plasticity function applied in the majority of plasticity models is not sufficiently accurate.

In this paper, the problem of high-rate deformation behaviour during high velocity micron-sized copper particles impacting against copper substrate is investigated numerically. Due to the lack of consistency in experimental data of strain rate exceeding the linear hardening threshold, the impact was simulated using four different plasticity models that envelope available experimental results.

This comparative study aims to illustrate numerically the ability of classical plasticity models to envelope experimental results by analysing and comparing different representative plasticity models. Additionally, a problem-specific model, accounting for both low and high strain rate sensitivity along the entire path of the loading, needs to be elaborated on and compared to classical models in describing the contact behaviour of a copper microparticle at high impact velocity. Copper was chosen as a suitable example for the calculations because it is a widely used spray material for which high strain rate material data are available.

The paper is structured as follows. In Section 2, the thermo-mechanical impact problem is outlined and the modelling domain is presented. In Section 3, the numerical approach as well as material properties used in the simulations are provided. Section 4 contains the results of the numerical simulation and discussion. The impacts are compared both on macro and micro levels. Finally, conclusions are drawn.

2. Theoretical background

2.1. Formulation of particle impact problem and description of the impact run

A micro-sized spherical particle of radius r strikes the copper substrate at high velocity v_0. The problem is described in Cartesian coordinates, the origin of which is located at the initial contact point. The particle moves along the vertical axis Oy, perpendicular to the plane and impacts the surface at the coordinate centre. Due to normal contact, the 3D problem is transformed to an axisymmetric one. The substrate is presented as a fixed hemisphere of radius R, where $R \gg r$. As a result, the 2D solution domain of the sphere-substrate contact is considered in the Oxy coordinate plane (Fig. 2a).

The physical nature of the particle-substrate interaction may be characterised in the following manner. Initially, the contact edge moves much faster than the elastic wave creating a shockwave. The created
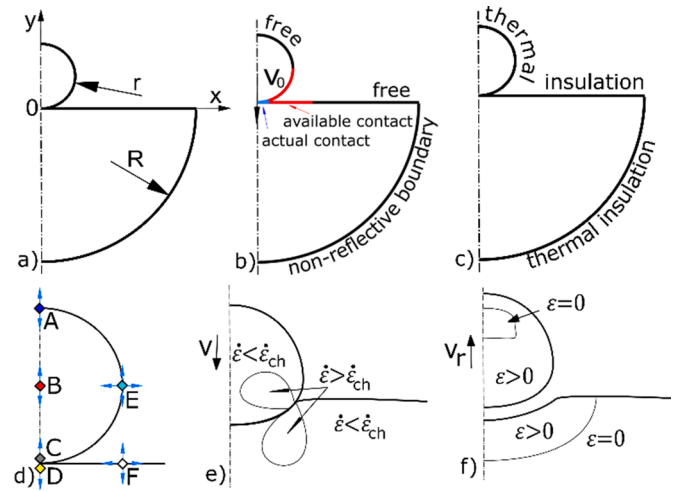

Fig 2. Illustration of the impact: solution domain (a), boundary conditions, mechanical (b) and thermal (c), control points with displacement directions (d), high strain rate zones during the loading phase (e) and geometry after rebound (f).

shockwave leads to concentration of stress exceeding initial yielding point in the early stage of the loading phase. The fully elastic stage of the loading is negligibly short compared to total impact time; therefore, it can be ignored when investigating the full interaction. The detailed experimentally visualised explanation of the shockwave phenomena was described by Field et al. [47]. Due to strain and strain rate hardening, the plastic zone increases until the particle reaches full plasticity (at lower velocities, part of the particle may remain elastic, as shown in Fig. 2f). The distortion of grain structure and the generation and glide of dislocations occur. The rest of the plastic work, is dissipated as heat energy. The ratio between resultant heat energy and plastic work performed is known as the cold-work conversion factor or the Taylor-Quinney coefficient [48]. Different studies show that the value of the coefficient tends to be higher for larger strain, even approaching full conversion [49]. The conversion coefficients used by other authors range from 0.5 [50] up to 1 [34]. The most commonly used coefficient value 0.9 is recommended by [31,51,32,52] and others. During the unloading phase, the decrease in yield stress due to a lower strain rate and thermal conduction, allows additional plastic deformations to take place because of residual stress.

2.2. Mathematical problem

The particle impacts the substrate at high velocity and heats up as a result of the dissipation of plastic energy. Since a material's plasticity model components (plastic strain, strain rate and temperature) change during impact, it is considered to be a nonlinear thermomechanical problem. The model consists of coupled equations of motion and heat transfer, see Eq. (1).

$$\begin{cases} \rho \dfrac{\partial^2 \boldsymbol{u}}{\partial t^2} = \nabla \cdot (F(\boldsymbol{u})S)^T + \boldsymbol{F}_V + \boldsymbol{F}_T & \text{(a)} \\[2mm] \rho C_p \dfrac{\partial T}{\partial t} + \nabla \cdot q = -\alpha T : \dfrac{dS}{dt} + Q & \text{(b)} \end{cases} \qquad (1)$$

The terms in Eq. (1a), from left to right, are: inertial forces, internal non-linear displacement-dependant forces (expressed by the deformation gradient tensor F and the second Piola-Kirchhoff stress tensor, which comprises nonlinear constitutive properties and may also depend on the temperature $S = S(\sigma_Y, T, \varepsilon, \dot{\varepsilon}, \dots)$) and external forces of mechanical and thermal nature. Similarly, for heat transfer, the terms in Eq. (1b) are: internal heat energy, heat flux, thermoelastic damping, and heat source from plastic dissipation. The two directional coupling is due

to the mechanical properties being dependant on the temperature and the heating of the material caused by plastic deformation. The heat balance equation is contributed by the dissipation power as a heat source.

The initial impact velocity is prescribed for the particle domain. Thermal behaviour is governed by the heat source occurring due to plastic deformation. With continued contact, large strain zones shift from the contact surface into the material bodies, forming two independent thermal sources in the particle and substrate.

The particle surface is divided into two parts, free external surface and contact surface. The mechanical boundary conditions shown in Fig. 2b, are defined on the surfaces of the particle and substrate. The contact surface depends on the contact history and the actual and available contact surfaces are distinguished. A surface-to-surface contact between the particle and the substrate is described using a penalty function with contact friction defined by Coulomb's Law [53]. To minimise the effect of reflected elastic wave, substrate domain is fixed using the low-reflecting boundary. The boundary lets waves pass out of the model by attempting to create a perfect impedance match for both pressure and shear waves [54].

Initially, both the particle and substrate sides of the contact deform equally, with the greatest strain located on the contact surface. Due to initial contact symmetry and short contact duration, heat transfer through the contacting surfaces, as well as surface heat flux, is ignored; all computational domain boundaries are considered to be thermally insulated. Thermodynamic boundary conditions are shown in Fig. 2c.

2.3. Characterisation of plasticity models

Before starting numerical analysis of the impact problem, a comparative analytical study of the plasticity models responsible for the local transition from elastic to plastic deformation in the copper was performed and the results of this study are presented in the following sections.

The deformation behaviour of the contacting partners undergoes elastic and elastic-plastic stages. The constitutive elastic relationship defined as non-linear relationship between increments of stress $d\sigma$ and strain $d\varepsilon$ as follows:

$$d\sigma = D_T(\sigma_Y, \varepsilon, \dot{\varepsilon}, T, \ldots)d\varepsilon. \tag{2}$$

Here, the elastic-plastic properties are defined by the tangential constant D_T, which accumulates the thermomechanical deformation history. Omitting the development of complicated plasticity relationships, the boundary between the elastic and plastic regions is defined by the plasticity criterion, governed by the yield stress value σ_Y.

The von Mises yield criterion, defined in terms of the von Mises equivalent stress σ_{eq} and the yield stress (strength) σ_Y, was determined by equation

$$\sigma_{eq}(\sigma_{ij}) = \sigma_Y. \tag{3}$$

Here, the equivalent stress stands for the stress intensity, i.e. the second invariant of the deviatoric stress, is expressed in terms of the components of the Cauchy tensor σ_{ij}. Originally, the von Mises plasticity model assumes perfect plasticity flow with a constant yield stress, equal to a material-specific constant: the yield stress $\sigma_Y = \sigma_0$. In reality, the yield stress is a quantity dependant on deformation history.

Yield stress is a variable quantity, usually contributed by strain ε, strain rate $\dot{\varepsilon}$ and temperature T. By assuming the independent contribution of all three parameters, the yield stress is presented as a multiplicative form of uncoupled functions [17]:

$$\sigma_Y(\varepsilon, \ \dot{\varepsilon}, \ T) = \sigma_0 \cdot f(\varepsilon) \cdot g(\dot{\varepsilon}) \cdot h(T). \tag{4}$$

Here, σ_0 refers to the yield strength or the stress corresponding to zero plastic deformation, $f(\varepsilon)$ represents an independent isotropic strain hardening function (in certain cases - work hardening); $g(\dot{\varepsilon})$ is the strain

rate hardening function, known as the dynamic increase factor (DIF), and $h(T)$ is the thermal softening function.

Strain hardening has been thoroughly investigated by many authors and can be obtained directly from the material stress-strain curve. For various materials, different hardening expressions are used. When solving dynamic elastoplastic problems involving metals, power law hardening described by the Ludwik (L) model is often used

$$\sigma_Y(\varepsilon) = \sigma_0 + B\varepsilon^n. \tag{5}$$

Here, B is the strain hardening coefficient and n is the strain hardening exponent.

Strain rate hardening is the most important factor that contributes to plastic yielding of the material for high-velocity impacts. The contribution of strain rate is reflected by different constants, the evaluation of which requires experimental justification.

For CS simulation, the J-C model is most-commonly used.

$$g_{JC}(\dot{\varepsilon}) = 1 + C \cdot \ln(\dot{\varepsilon} / \dot{\varepsilon}_0) \tag{6}$$

Here C is the strain rate hardening coefficient, $\dot{\varepsilon}$ is the strain rate, and $\dot{\varepsilon}_0$ is the reference strain rate.

The popular power law C-S model (7) is more strain rate-sensitive at higher strain rate values.

$$g_{CS}(\dot{\varepsilon}) = 1 + D(\dot{\varepsilon}/\dot{\varepsilon}_0)^k \tag{7}$$

Here D is the strain rate hardening coefficient and k is the strain rate hardening exponent.

Temperature softening for copper can also be described simply by the J-C power law (8),

$$h(T) = 1 - T_*^m, \tag{8}$$

which is the most popular model for temperature-dependant plasticity, properly describing the behaviour of copper up to 500°C [55]. Here m is the temperature softening exponent and T_* is the relative temperature calculated as

$$T_* = \frac{T - T_{ref}}{T_m - T_{ref}}, \tag{9}$$

where T is the absolute temperature, T_m is the melting temperature, and T_{ref} is the reference temperature. In this paper, different strain rate sensitivity models are used, in combination with Ludwik strain hardening and Johnson-Cook thermal softening functions.

3. Methods and materials

A single micro-sized copper particle (with radius $r = 20$ μm) impacting a plain surface substrate was numerically investigated. The particle impacts the substrate with a velocity ranging from 300 to 500 m/s. The solution domain comprised two radial sections of particle and substrate. The substrate was modelled as a half sphere with radius $R = 200$ μm. The computational setup is shown in Fig. 2a.

This section contains a description of the numerical finite element (FE) model, material parameters, and the constants of selected plasticity models used in the simulations.

3.1. Finite element approach

The mathematical model of the thermomechanical problem described by Eq. (1) was implemented using COMSOL Multiphysics FE code [56] with large strain, displacement and material nonlinearity. Due to the axially symmetrical character of the impact, the model was simplified as axisymmetrical, to reduce computation time.

The friction-slide contact between the particle and substrate was assumed. It is described using a penalty function with contact friction defined by Coulomb's law. Additional study was performed to evaluate the influence of friction, coefficient values between 0 and 1 were tested.

It was found that coefficient of friction (COF) has no noticeable influence on macroscopic variables of impact, while its influence on contact surface displacement varies around 5% (Fig. 3). Low influence of COF considering CS impact at 500 m/s velocity was demonstrated by [57]. The friction coefficient of dry copper on copper was assumed to be $\mu = 1$ [58].

The nonlinear properties of constitutive materials are reflected by different yielding models. The strain rate sensitivity models were implemented as modifier functions for the L strain hardening and J-C thermal softening models, which are already built into the FEA software.

For computational purposes, the 2D solution domain was discretised by applying two types of meshing technique (Fig. 4). The larger part of the solution domain was covered by an irregular mesh, applying six-node triangular elements. For a description of the contact zone and areas of large deformation, a high-quality regular mesh of eight-node serendipity quadrilateral elements was used.

The quality of the FE mesh was tested by changing the ratio of the contact element size a to the particle radius r. After several preliminary impact simulations, the nominal meshing size for contact elements $a = 0.031 \cdot r = 6.2 \cdot 10^{-7}$ m was selected. The minimum element size was chosen to prevent the contact surface rippling from causing secondary contacts that would need finer time-stepping in the simulation.

Mesh quality was evaluated by element skewness, which is the default quality measurement in COMSOL. Mesh data are given in Table 1.

3.2. Material properties

This subsection contains description of copper properties used in numerical simulation and selection procedure of plasticity constants. Evaluation of strain rate plasticity parameters in the high velocities and their relation with experimental data is discussed in details. The analysis of experimental strain rate data is used to explain the inefficiency the inefficiency of classical plasticity models in describing high strain rate plasticity. Development of new model increasing adequacy to experiments is also discussed.

3.2.1. Basic copper parameters

Since the particle size is close to the scale of the crystal structure of uniform pure copper, the homogenous material is used for numerical simulations. Basic material parameters for copper have been extensively investigated and documented by many authors; they can be found in encyclopaedic databases. Temperature-dependant material parameters [59] were used and their values are given in Table 2.
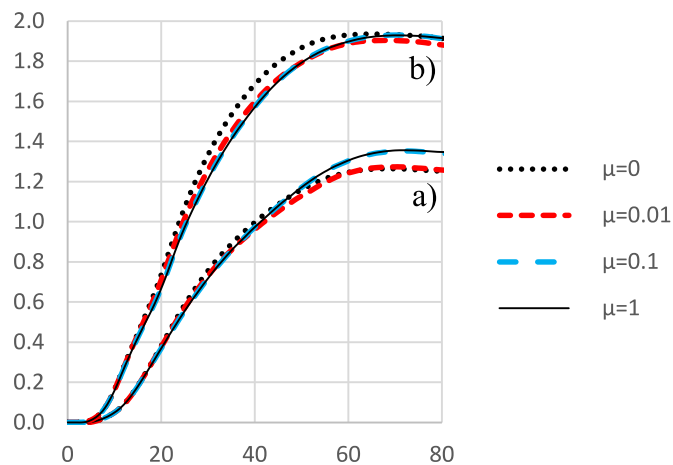

Fig 3. Displacement of substrate surface points in radial direction using different friction coefficients. The point distance from impact centre a) 20 μm, b) 15 μm.

Methods to obtain the elastic parameters of the material are simple and well-known. In order to obtain plasticity parameters, more complicated methods were used.

3.2.2. Strain hardening and temperature softening parameters

The constitutive properties of the elastoplastic material are basically defined by the yield conditions; therefore, the initial yield stress and other state-dependant parameters must be experimentally confirmed. The yield stress was obtained directly, by static tensile-compression and shear experiments, and indirectly, by indentation experiments. In indentation experiments, the material hardness was obtained. In the literature, hardness is compared to yield strength with a Tabor factor of 3 [60,61] (10).

$$3\sigma_Y = \sigma_H \tag{10}$$

The parameter values describing copper strain hardening and thermal softening were selected from CS particle impact simulations [31–33] and are shown in Table 3.

Data from strain hardening and temperature softening plasticity models were used, in combination with strain rate models.

3.2.3. Strain rate parameters

Strain rate hardening is the most important factor that contributes to the plastic yielding of the material for high-velocity impact. The contribution of strain rate is reflected by different constants, the evaluation of which requires experimental justification.

A characteristic feature of the strain rate plasticity is the two-segmented relation between yield stress and strain rate [41]. Low strain rate hardening results, obtained by Follansbee and Kocks [46] and later verified by many experiments, display only a slight increase in material hardening, up to 10^4 s^{-1} strain rate.

For higher strain rate results, specific experimental techniques were needed. When considering copper, several experimental techniques could be mentioned. Recently, experimental results using shock compression were obtained by Meyers et al. [62] and Murphy et al. [63]. The results from pressure shear were obtained by Tong et al. [64]. Here, the shear strength was measured. For a comparison of the experimental results, shear strength σ_S and yield stress σ_Y were used, assuming their proportional value as follows

$$2\sigma_S = \sigma_Y. \tag{11}$$

Additional strain rate hardness results, obtained via laser induced particle impact tests by Hassani et al. [65], give a material dynamic hardness result. An evaluation of high strain rate sensitivity by molecular dynamics simulations was attempted by Bringa et al. [66]. The distribution of the experimental strain rate results is shown in Fig. 5.

However, due to experimental difficulties, a systematic view is absent. Therefore, in this paper, few plasticity models are selected for comparison.

The parameters of the plasticity models are selected according to the experimental results. However, compared to static experiments, strain rate hardening experiments are much more difficult to perform, especially at higher strain rates. The original results for the strain rate-dependant copper properties were published by Follansbee and Kocks [46]. These results show the yield stress as a function of strain rate at a fixed value of the uniaxial strain. The plotted graph presents two-segmented relationship with a threshold value around 10^4–10^5 s^{-1}. Here the rapid increase in yield strength is attributed to thermal activation. The first low-rate sensitivity regime below the threshold is almost constant throughout the deformation. Its values have since been reproduced by numerous experiments, including widely applied and revised Split Hopkinson pressure bar tests [67]. The second regime of high-rate sensitivity above the threshold is characterised by a rapid increase in strain rate sensitivity, near the limits of the experimental range. Due to experimental difficulties, a systematic view is absent, but several scattered results of high strain rate sensitivity have been
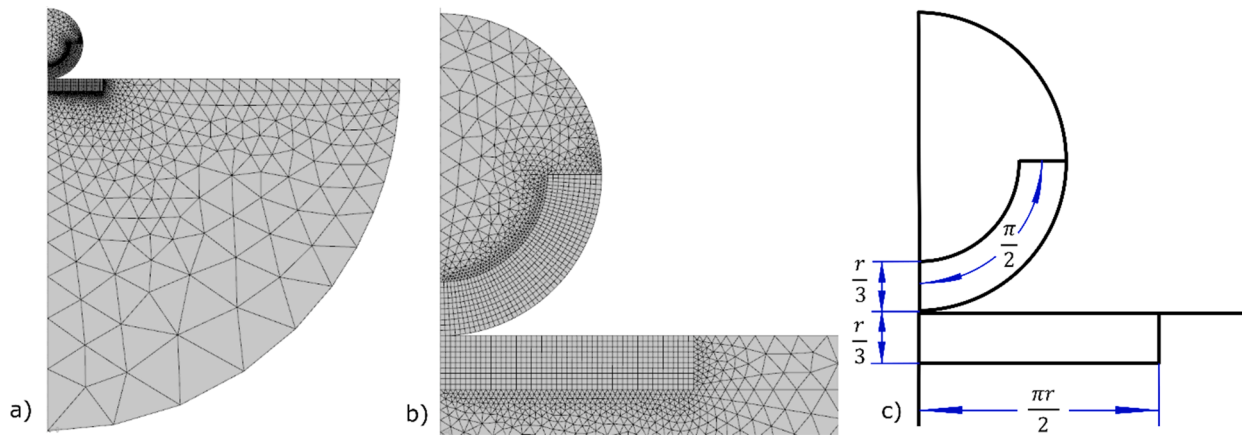
Fig 4. Illustration of an FE mesh used for simulations: general view (a); refined area of contact zone (b); geometry of the refined area (c).

Table 1
FEA mesh data.

Description	Value
Quadrilateral elements (number of elements)	1000
Triangular elements (number of elements)	2270
Minimum quality of quadrilateral elements (skewness)	0.99
Average quality of quadrilateral elements (skewness)	0.9946
Minimum triangular element quality (skewness)	0.5803
Average quality of triangular elements (skewness)	0.8539

Table 2
Basic temperature-dependant copper parameters.

Parameter, Unit	Notation	Range of values for 20–500 °C
Density, kg/m^3	ρ	8950–8700
Elastic modulus, GPa	E	125–105
Poisson ratio	ν	0.335
Specific heat, J /(kg·K)	C_p	385–425
Thermal conductivity, W /(m·K)	λ	395
Coefficient of thermal expansion, K^{-1}	α	1.65–1.8 (10^{-5})

Table 3
Copper strain hardening and thermal softening parameters.

Model	Parameter, Unit	Notation	Values
Ludwik (Eq. (5)) (strain hardening)	Initial yield stress, MPa	σ_0	90
	Strain-hardening coef., MPa	B	292
	Strain-hardening exponent	n	0.31
Johnson-Cook (Eq. (8)) (temperature softening)	Thermal softening exponent	m	1.09
	Melting temperature, K	T_m	1358
	Reference temperature, K	T_{ref}	293

presented by various authors [62–66].

Higher strain rate results (ranging from 10^4 to 10^7 s^{-1}) were obtained from pressure shear experiments by Tong et al. [64] and Meyers et al. [62]. High strain rate results (ranging from 10^6 to 10^9 s^{-1}), acquired by the laser-induced particle impact test (LIPIT), can be found in Razavipour and Jodoin [34], and Hassani et al. [65] papers. Using the shock compression experiment, additional strain rate sensitivity data at the 10^{10} s^{-1} strain rate was acquired by Murphy et al. [63]. However, in these experiments material undergoes a wide range of strain rates,
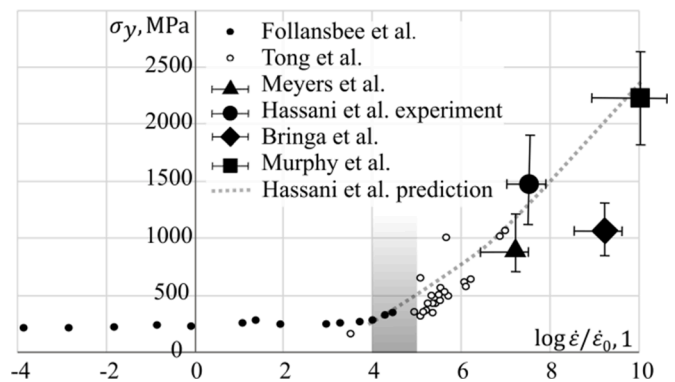

Fig 5. Illustration of experimental results on copper strain rate hardening.

therefore hardening value obtained for the characteristic strain rate is only applicable for the experiment.

Since the J-C model is logarithmic, it describes the strain rate sensitivity well at lower strain rate values, up to 10^4 s^{-1}. However, this model cannot describe the rapid increase in strain rate sensitivity at higher strain rates that occur during high-velocity contact.

J-C material parameters for strain rate hardening were obtained from the same literature as the strain and temperature-dependant parameters.

The power-law C-S model can be used to describe strain rate sensitivity at higher strain rates. Nevertheless, this model cannot describe the break point in experimental results that separates low and high-strain rate sensitivities and, therefore, is only accurate in a short range of high-strain rates.

The C-S model in this paper is suited to Hassani's experimental results.

The strain rate-independent model, addressed as the Ludwik (L) model in this paper, is defined by a constant DIF value for all strain rates during impact. Therefore, the DIF value is selected so that it corresponds to the impact's characteristic strain rate.

The L model is also suited to Hassani's experimental results. It is described by a DIF value of 3.35, for the characteristic strain rate 7.5·10^6s^{-1} of the simulated impact.

3.2.4. Elaborated two-function combined model

The characteristic strain rate of impact exceeds the threshold value between low and high strain rate sensitivity regimes. Therefore, to better describe strain rate sensitivity, different strain rate-dependant models, that can describe experimental results at both low and high strain rates, as well as the break point in between, should be used. However, none of the classical models can adequately meet these requirements. For this

reason, a combination of two modified models for high and low-strain rate sensitivity regimes was used (12).

$$g(\dot{\varepsilon}) = \max\left(1 + C\ln(\dot{\varepsilon}/\dot{\varepsilon}_0 + 1), F + D_1(\dot{\varepsilon}/\dot{\varepsilon}_0)^{k_1}\right) \qquad (12)$$

Here, the modified J-C model, Eq. (6), was used to describe the low strain rate sensitivity. Modification was needed to prevent negative DIF values at very low strain rates.

The high strain rate sensitivity is described by the modified C-S model Eq. (7). The simple modification, by a negative value of F, was used to set the intersection between models.

The coefficients for the two-function combined (TFC) model were chosen to suit the model for the Follansbee, Mayers, Tong, and Murphy experimental results.

The strain rate sensitivity parameter values used for simulations in this paper are presented in Table 4.

Graphic representations of the J-C, C-S, L and suggested TFC models, as well as the distribution of experimental strain rate hardening results for copper, are shown in Fig. 6. Initial yield stress $\sigma_1 = \sigma(\varepsilon, T)$ was calculated for $\varepsilon = 0.15$ strain and room temperature $T = 20\,°C$.

Fig. 6 shows the strain rate sensitivity of the models used in this paper, as well as the experimental and simulation results from different papers.

4. Numerical results and discussion

Numerical results were obtained by using the thermomechanical model described (Eq. (1)) and applying four selected strain rate sensitivity models. The impact time history was analysed using parameters (such as resultant displacements, velocities and forces) describing the behaviour of the entire particle as a whole, as well as local state variables (describing the state of specified points, displacements, strain, strain rate and temperature).

### 4.1. Analysis of particle variables

The motion of a particle in time can be represented in different ways. The resulting particle motion is described by global parameters, such as the average displacement and velocity of the particle mass and contact forces.

4.1.1. Displacement

Particle displacement is characterised by the average displacement of particle mass, equivalent to the displacement of the particle's centre of mass. In the case of a deformable particle, displacement of the particle's centre of mass is not equal to the displacement of the particle's centre point. This difference strongly depends on the deformed shape of the particle and the different plasticity models used. The average displacements reflect the differences between the 'characteristic hardness' of the plasticity models.

Table 4
Copper strain rate (S-R) hardening parameters.

| Model	Parameter, Unit	Notation	Values
Johnson-Cook (Eq. (6))	S-R hardening coef.	C	0.025
	Reference S-R, s^{-1}	$\dot{\varepsilon}_0$	1
Cowper-Symonds (Eq. (7)) (selected by author)	S-R hardening coef.	D	0.19
	S-R hardening exp.	k	0.18
Combined model (Eq. (12)) (selected by author)	S-R hardening coef.	D_1	3
	S-R hardening exp.	k_1	0.068
	Modifier	F	−5.5
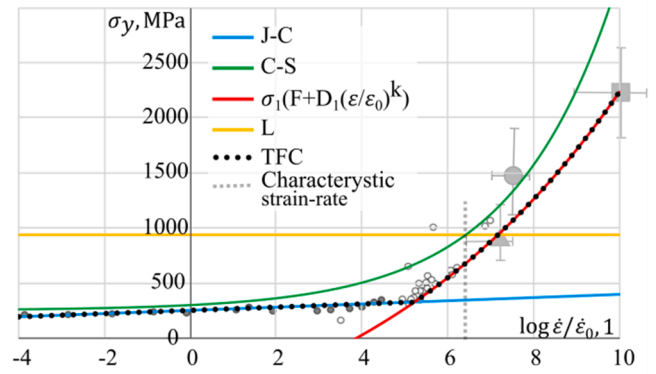
Fig 6. Illustration of copper strain rate hardening models used in later simulations compared to experimental results.

The computational results, represented in terms of the average particle displacement, are presented in Fig. 7. A comparison of different plasticity models obtained at an impact velocity of 300 m/s (Fig. 7a) illustrates that the average particle displacement is greater for plasticity models with lower strain rate sensitivity. It is obvious that the C-S and the L models have similar displacement characteristics because of similar yield stresses at the impact characteristic strain rate $\dot{\varepsilon}_{ch} = v_0/d_p = 7.5 \cdot 10^6 \ s^{-1}$. It appears that, for different plasticity models, the maximum indentation time is related to the indentation depth.

The contribution of impact velocity to the TFC model at velocities of $v_0 = 300, \ 400$ and $500\,m/s$, are shown in Fig. 7b. Here, the average displacement of the particles follow a proportional relationship with the impact velocity. The figure shows that the maximum penetration time is practically insensitive to impact velocity.

4.1.2. Velocity

Particle velocity is characterised by the average velocity of particle mass, equivalent to the velocity of the particle's centre of mass. It is an important parameter that reflects loading and contact duration. The end of the loading phase is characterised by zero average velocity. The particle rebound velocity is used to evaluate kinetic energy dissipation, as well as the coefficient of restitution, which is calculated as the ratio between rebound and impact velocities.
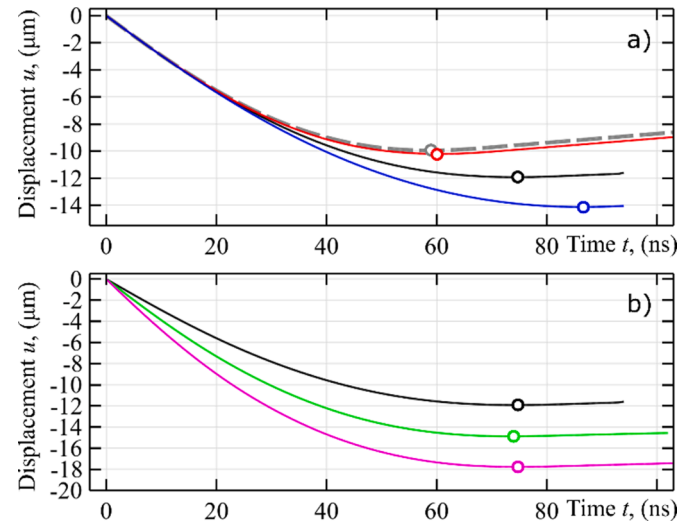
Fig 7. Variation of the average particle displacement vs. time: comparison of different plasticity models (red - L, blue - J-C, gray - C-S and black - TFC) at 300 m/s (a); and TFC model at different velocities (black - 300, green - 400 and magenta - 500 m/s) (b).

Variations of the average particle velocity over time are presented in Fig. 8. The graphs in the figure are structured similarly to the displacement graphs in Fig. 7. From the graphs in Fig. 8a, it follows that the loading phase duration is different for different plasticity models. Similarly, with maximum displacement, the duration is longer for lower DIF plasticity models. When observing average displacements, we can see that the average velocity value of the L and C-S models is similar. Rebound velocity at the end of the contact is higher for plasticity models with higher DIF.

The contribution of impact velocity to the average particle velocity is shown in Fig. 8b. Here, the dependency of the loading duration on the impact velocity is insignificant. Rebound velocity is similar for the observed cases. However, the similarity may be attributed to different types of particle-substrate separation, as will be shown in Section 4.2.2.

4.1.3. Contact force

The time history of the contact force, as well as the contact pressure distribution for different time steps, is shown in Fig. 9. The computation results, obtained by applying different plasticity models under $v_0 = 300$ m/s impact velocity, represented in terms of the contact force, are presented in Fig. 9a. The maximum contact force is reached well before maximum indentation. For most of the models, the maximum contact force is reached around the middle of the contact duration. Differences in unloading can be seen between the C-S and L models.

In the L model (Fig. 9b), we can see that the contact force increases with the contact surface area, in terms of contact pressure distribution. On the other hand, in the TFC model (Fig. 9c), while the contact area increases, the average contact pressure decreases as a result of the decreasing strain rate.

4.2. Local-State variables

The quantitative differences seen in the Section 4.1 can be explained by the physical nature of impact behaviour. During impact, a particle deforms irregularly.

4.2.1. Deformation

The history of particle shape deformation can be simply characterised by tracking the displacements of selected control points. The computational results, represented in terms of particle control point displacement, obtained by applying different plasticity models under
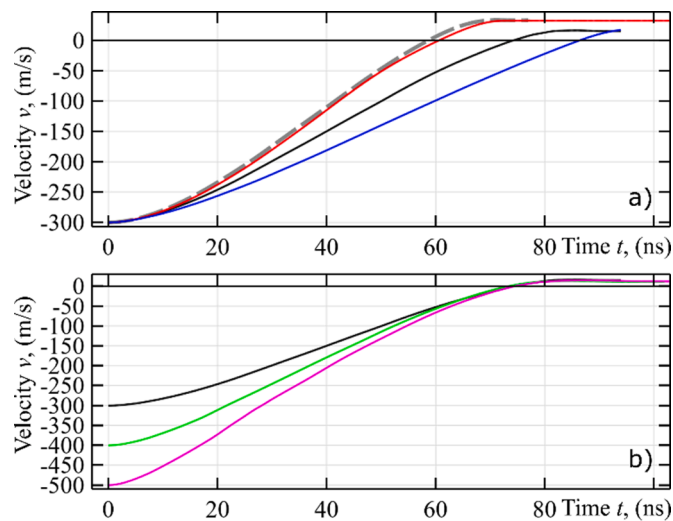

Fig 8. Average particle velocities vs. time: comparison of different plasticity models (red - L, blue - J-C, gray - C-S and black - TFC) at 300 m/s (a); TFC model at different velocities (black - 300, green - 400 and magenta - 500 m/s) (b).

300 m/s impact velocity, are presented in Fig. 10.

From the displacement graphs, it can be seen that the highest and lowest displacements are at the top of the particle and contact points (A and C); the difference between these displacements shows particle flattening. Similarly, differences between A-B and B-C show unequal flattening of the particle's upper and lower hemispheres. L, J-C, and our models also show that the displacements of the middle point (B) of the particles and the displacements of the equator point (E) differ due to the increase in the contact surface approaching the equator. Despite the previous similarity of the average displacement between the L and C-S models, it can be seen that the latter model has identical displacement for the aforementioned control points. In all cases, average displacements stay between the centre and equator point displacements.

In all of the investigated cases, during contact, the average velocity of the particle is at least double the velocity of the contact points, resulting in the indentation value being lower than the particle flattening.

To evaluate the change of contact area characterised by friction slip, as well as the shifting contact edge, the displacements of contact surfaces in the radial direction are observed. The computational results presented, in terms of the contact surface (between points C-E and D-F in Fig. 2d) radial displacements at time intervals, are shown in Fig. 11. Each figure contains results obtained by applying different plasticity models under a 300 m/s impact velocity, as well as the TFC plasticity model at different impact velocities.

All strain rate-dependant models show that the maximum displacement of the particle is located at the edge of contact. The sharp edge of the substrate contact zone appears due to particle-substrate contact friction. It is observed that the radial displacements of the substrate surface are lower than the particle surface displacement, suggesting uneven strain of the contact surfaces. The sudden divergences between the contact displacement of the particle and the substrate seen in Figs. 11a and 11f, suggest local slipping of the surfaces that appear early in the contact. Some shape similarities can be seen between the J-C model at 300 m/s and the TFC model at higher velocities.

Formation of the indentation can be observed by normal displacement of the contact surface. The computational results representing the substrate surface's normal displacements at time intervals, are presented in Fig. 12. The graphs in the figure are structured similarly to the displacement graphs in Fig. 11.

It is evident that models with higher strain rate sensitivity exhibit a decrease in positive substrate displacement during contact. In the case of the C-S model (Fig. 12c), at the end of the impact there is no observable positive displacement. Similar results can be seen in the Razavipour and Jodoin [34] simulations at lower impact velocities. Less strain rate-dependant models exhibit a sharper edge to their indentation profile. In the case of the L model (Fig. 12a), where the material strength does not reduce at the end of contact, large displacements can be seen after unloading.

While examining the displacements of control points and surfaces during contact, it has been noted that the particle-substrate impact duration can be observed differently. All models show that the contact point reaches the maximum impact depth much earlier than other particle points and, by comparing the radial displacements of the particle and substrate surfaces, we see that the substrate deformation stops earlier than particle deformation.

4.2.2. Equivalent plastic strain

Not only does the yield stress depend on strain hardening, but strain itself is dependant on the plasticity model used. The strain at the end of the contact shows a clear difference between plasticity models. The computational results representing the distribution of the equivalent plastic strain are presented in Fig. 13.

All of the models exhibit a large strain located closer to the edge of the contact surfaces. The J-C model (Fig. 13b) exhibits a larger plastic deformation, due to the lower overall material yield stress during high-
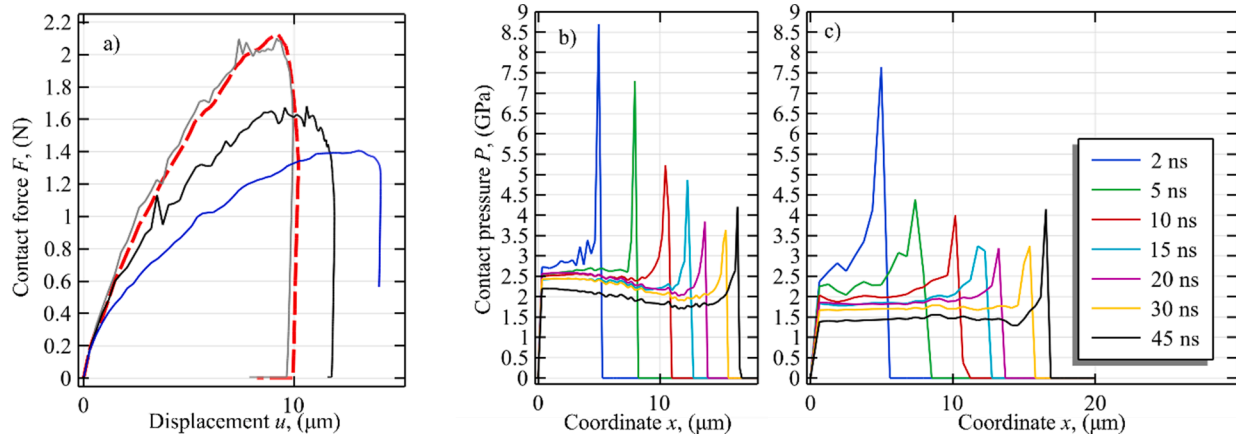
Fig 9. Illustration of the contact force vs. time for different plasticity models (red - L, blue - J-C, gray - C-S and black - TFC) at 300 m/s (a); contact pressure distribution for strain rate-independent L model (b) and TFC model (c) at different time instances.
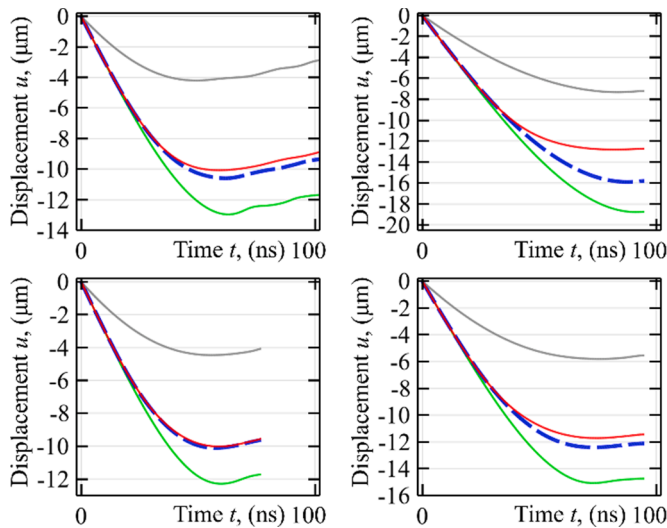
Fig 10. Time histories of normal displacements u(t) of control points (green - upper point A,
red - center point B, gray - contact point C and blue - equator point E) at 300 m/s, obtained by different plasticity models: L (a), J-C (b), C-S (c) and TFC (d).

strain rate deformation. The similarity between the J-C model at 300 m/s and our model at 400 m/s impact velocity can be seen once again. In the L model (Fig. 13a), we can see higher concentrations of localised strain due to the absence of strain rate hardening, which otherwise prevents such localisation.

The difference in the manner of the particle-substrate contact separation can be seen for the TFC model at different impact velocities. For a lower impact velocity, contact separation starts at the edge of the contact surface, while for a higher velocity impact, separation starts at the initial contact point.

4.2.3. Equivalent strain rate

During impact, the material undergoes deformation at extremely high deformation rates. Any effect of a strain rate sensitivity model on strain rate distribution or total value should be noted. The average strain rate in the particle is easy to obtain. However, more precise substrate strain rate values can only be evaluated using specified zones. For example, in Fig. 14, the following values are shown:

1 Average strain rate inside a fixed-size sphere around an initial contact point (average strain rate for the particle-size sphere is shown)

2 Average strain rate of the plastic zone (where $\varepsilon > 0$, as shown in Fig. 2f);
3 Average strain rate of the active plastic zone (where $\dot{\varepsilon} > 0$).

As we can see from Fig. 14, different interpretations of strain rate in the substrate gives different results. Therefore, in Fig. 15, the average strain rate is only presented for the particle and the substrate strain rate can be estimated from the strain rate colour plot given in Fig. 16.

The computational results representing average strain rate of the particle volume are presented in Fig. 15. Here, we can see that only the impact loading stage is characterised by high strain rates. It is also seen that the L model exhibits a greater strain rate than strain rate-sensitive models, except for the (overall) 'softer' J-C model. The average strain rate for the J-C model during 300 m/s impact almost reaches the calculated characteristic strain rate value $7.5 \cdot 10^6$ s^{-1}. With an increase in impact velocity, the maximum value of the average strain rate approaches the characteristic value.

The strain rate near the contact edge is at least five times the characteristic value and the large difference between the highest and lowest strain rate needs to be represented at a logarithmic scale, as shown in Fig. 16. Despite the other differences, strain rate distribution is similar for all models. We can also see that local strain-rates obtained during impact exceeds strain rate limits of most dislocation-based plasticity models.

4.3. Temperature

Around 90% of the initial kinetic energy of the system is converted to heat energy during contact, while remaining kinetic and elastic strain energy is negligible; however, this does not increase the average particle and substrate temperature by much. The average particle temperature is shown in Fig. 17.

Fig. 17 shows that the models with higher yield stress, due to strain rate sensitivity, generate more heat energy from impact even when they have a lower average strain. The L model generates less heat energy due to a higher yield stress, allowing the particle and substrate to store more residual elastic energy. It can be seen that the generated heat energy increases with impact velocity. However, if we assume that contact reaches the melting temperature at the adhesion condition in CS, localised temperature distribution should be observed. The temperature distribution is shown in Fig. 18.

The contact in the L model (Fig. 18a) heats up more due to a higher local strain concentration. The local temperature of the particle is higher compared to the substrate. With increasing impact velocity, the temperature of the contact zone increases rapidly.
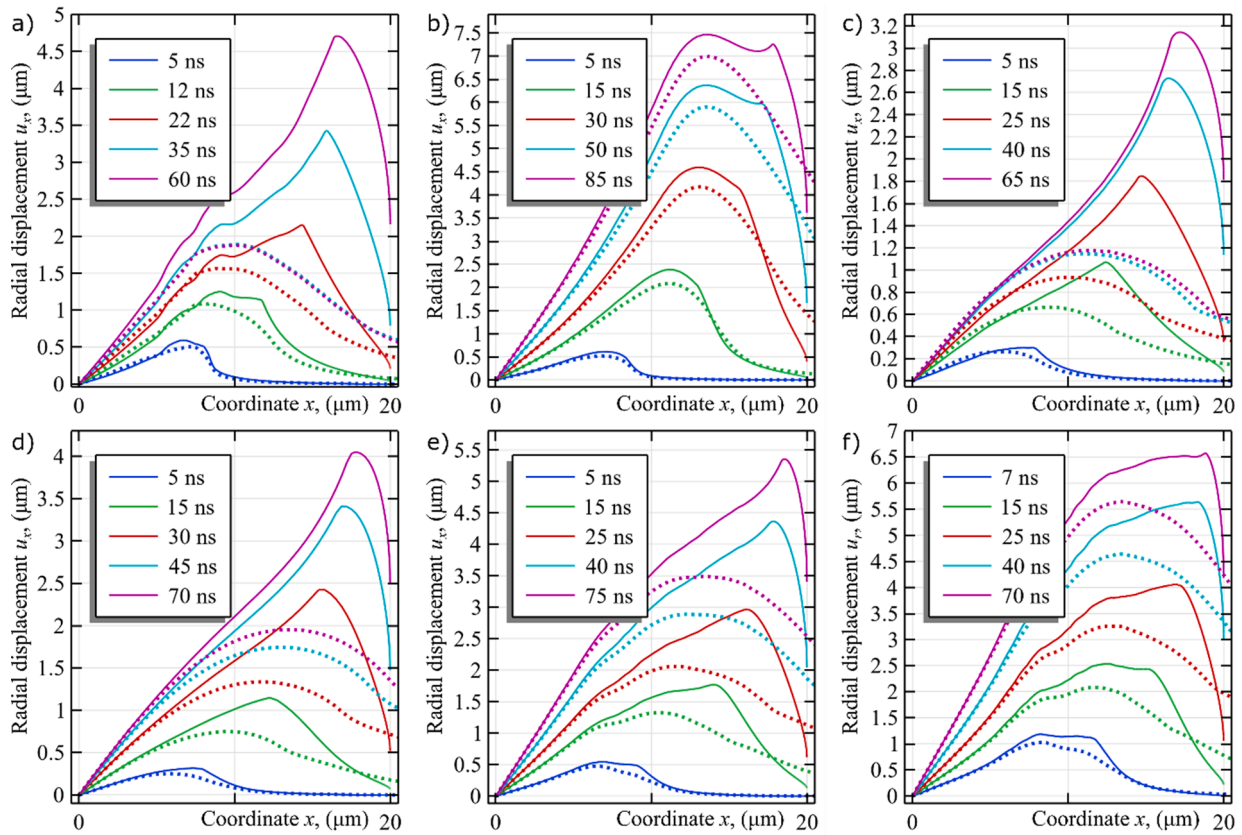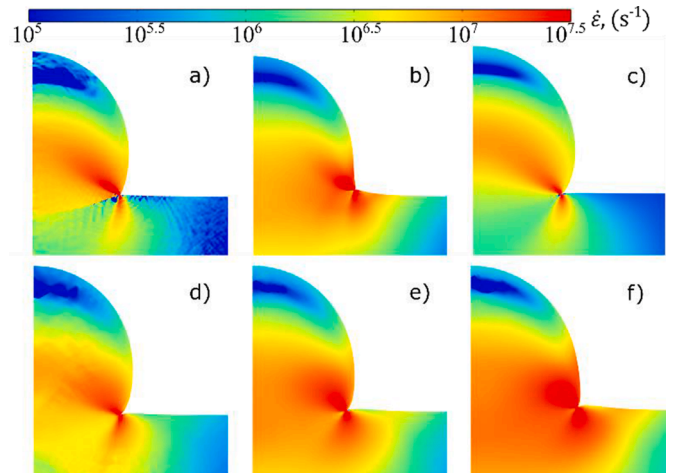
Fig 11. Particle (shown as a solid line) and substrate (shown as a dotted line) contact surface displacement in a radial direction at 300 m/s impact velocity using four different plasticity models: L (a), J-C (b), C-S (c) and TFC (d); as well as the TFC model at 400 (e) and 500 (f) m/s.
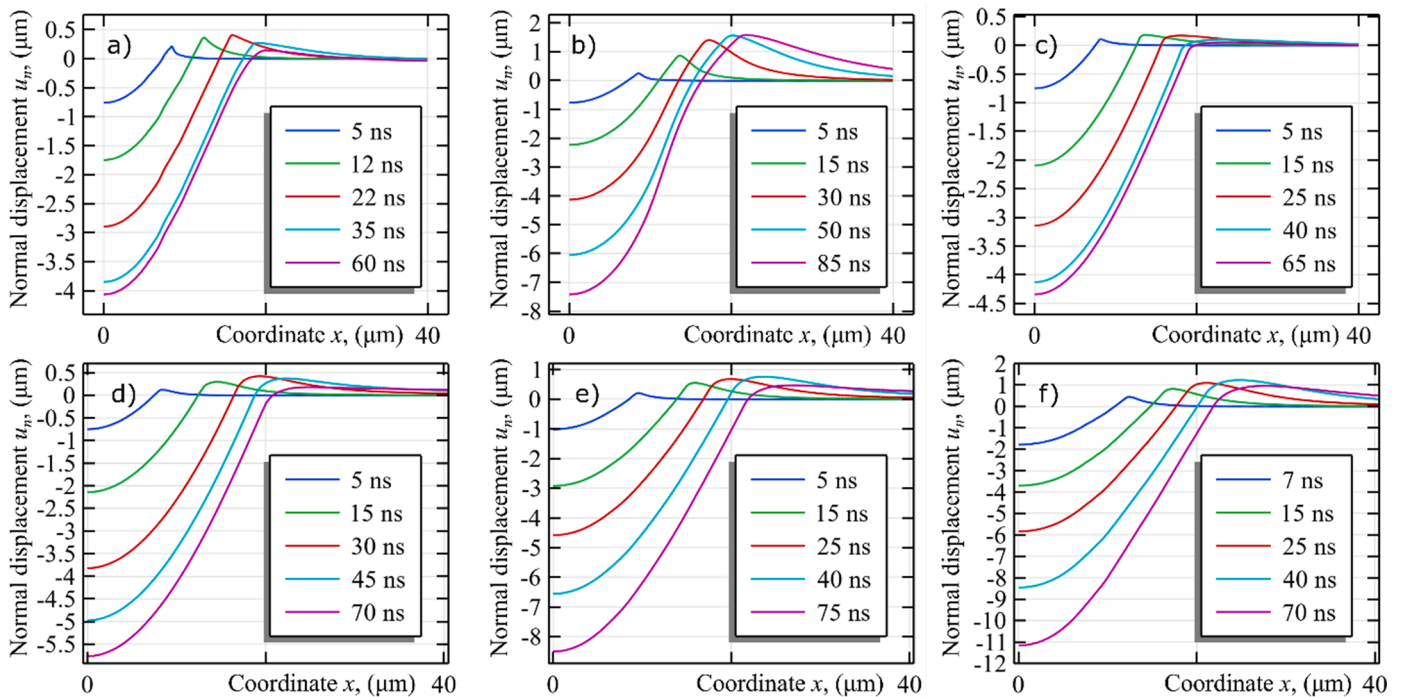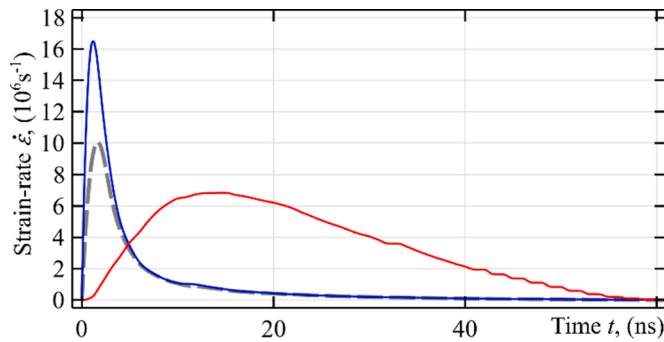

Fig 12. Illustration of substrate surface displacement in normal direction at 300 m/s impact velocity using four different plasticity models: L (a), J-C (b), C-S (c) and TFC (d); as well as the TFC model at 400 (e) and 500 (f) m/s.
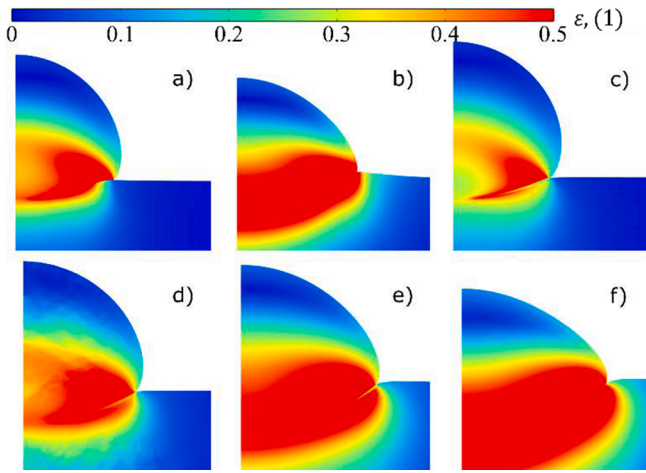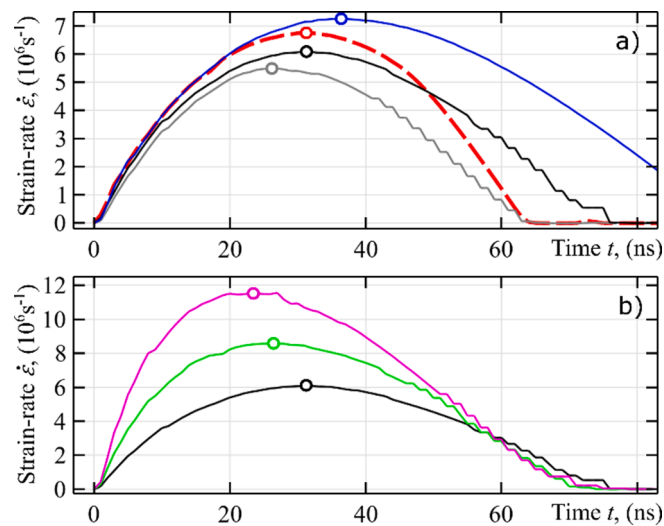
Fig 13. Colour plot of the strain for the particle and the substrate after rebound obtained by different plasticity models: L (a), J-C (b), C-S (c) and TFC (d, e, f). Velocity was 300 (a, b, c, d), 400 (e), and 500 (f) m/s.


Fig 14. Three interpretations of an average strain rate on the substrate (red - for a particle sized sphere, gray - for the plastic zone and blue - for the active plastic zone).

Fig 15. Illustration of the average particle strain rate vs. time: for different plasticity models (red - L, blue - J-C, gray - C-S and black - TFC) at 300 m/s (a); and TFC model at different velocities (black - 300, green - 400 and magenta - 500 m/s) (b).

Fig 16. Color plot of the strain rate for the particle and substrate at the time instant of the maximum average strain rate, obtained by different plasticity models: L (a), J-C (b), C-S (c), and TFC (d, e, f). Velocity is 300 (a, b, c, d), 400 (e), and 500 (f) m/s.
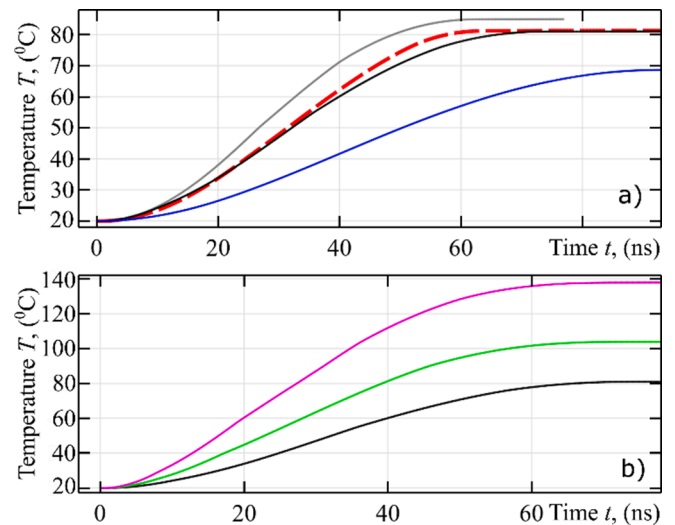
Fig 17. Illustration of average particle temperature during impact for different plasticity models (red - L, blue - J-C, gray - C-S and black - TFC) at 300 m/s (a) and TFC model at different velocities (black - 300, green - 400 and magenta - 500 m/s) (b).

4.4. Yielding

The average yield stress of the material changes during the simulation. The computation results, represented in terms of the average particle yield stress, are presented in Fig. 19. The graphs in the figure are structured similarly to the earlier two figures.

Fig. 19a shows that the L model has a higher yield stress compared to the C-S model but only at the beginning of the loading phase and during the unloading. The material modelled with the J-C model is much 'softer' during contact. The yield stress increases with impact velocity, as seen in Fig. 19b, and is caused by both higher strain and strain rate.

For a clearer picture, independent contributions of each parameter during contact can be expressed as non-dimensional time-dependant functions of strain - $f(\varepsilon(t))$, DIF - $g(\dot{\varepsilon}(t))$ and temperature - $h(T(t))$. Their average values in particles are shown in Fig. 20. Each figure contains results obtained by applying different plasticity models under $v_0 = 300$ m/s impact velocity.

It can be seen that, for the J-C model, strain rate hardening only
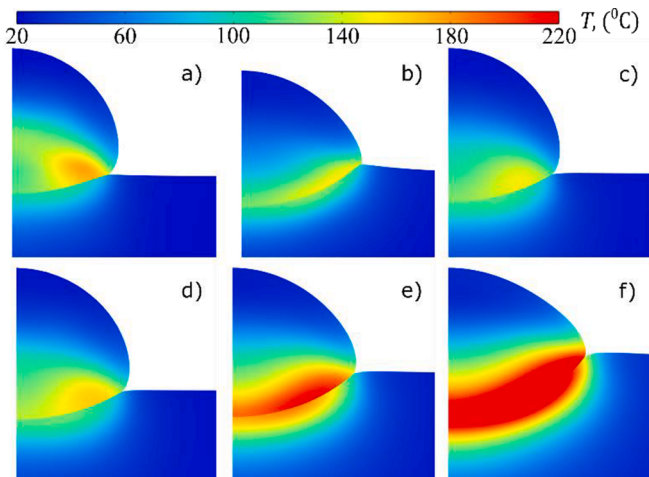
Fig 18. Color plot of temperature field for particle and substrate at the time instant of maximum indentation, obtained by different plasticity models: L (a), J-C (b), C-S (c) and TFC (d, e, f); Velocity 300 (a, b, c, d), 400 (e) and 500 (f) m/s.
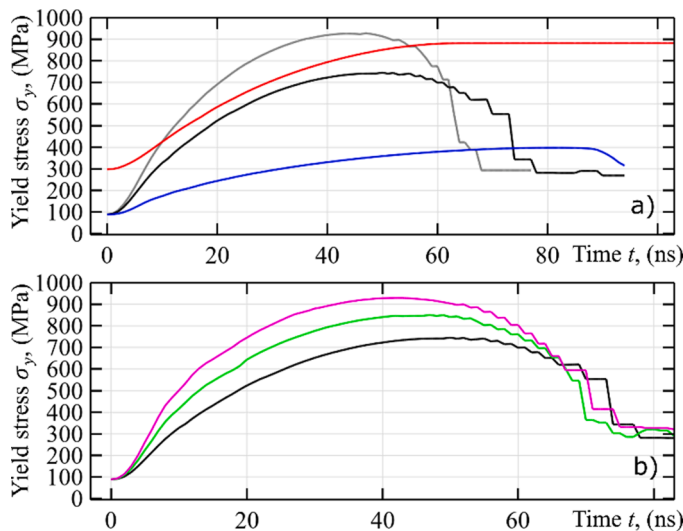

Fig 19. Illustration of average particle yield stress during impact for different plasticity models (red - L, blue - J-C, gray - C-S and black - TFC) at 300 m/s (a), and TFC plasticity model at different velocities (black - 300, green - 400 and magenta - 500 m/s) (b).

accounts for a small increase in yield stress. The increase in temperature has almost no effect on average particle yield stress. During contact, the average reduction of the yield stress due to temperature reaches around 1%. The local yield stress decrease near contact reaches up to 6% and 12% for impact velocities of 300 m/s and 500 m/s, respectively. To better evaluate local temperature and its contribution at deposition velocity, a finer mesh should be used.

5. Conclusions

The problem of rate-dependant plastic contact deformation occurring during a high-velocity impact of copper particle vs. copper substrate was considered by applying the continuum-based formulation and finite element thermomechanical analysis. Emphasis is given to the illustration of the applicability of different plasticity models undergoing a wide range of strain rates (including low and high strain rate sensitivity ranges) during the impact. The analytical study of the continuum-based plasticity models was performed, and representative models of Johnson-
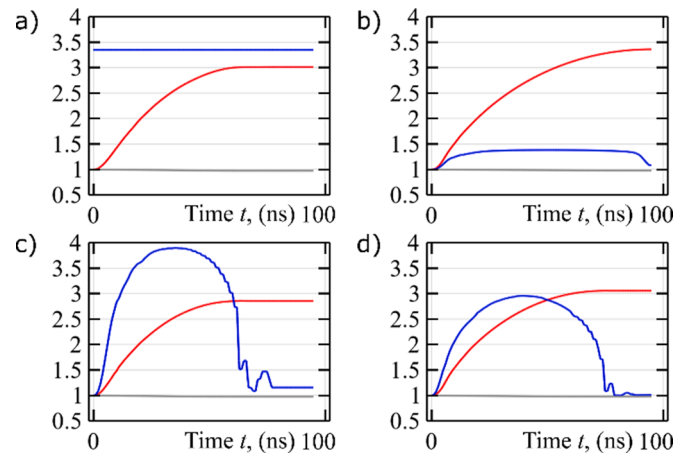
Fig 20. Time histories of the yield stress component (red - $f(\varepsilon(t))$, blue - $g(\dot{\varepsilon}(t))$, gray - $h(T(t))$) contribution to average particle yield stress at 300 m/s, obtained by different plasticity models: L (a), J-C (b), C-S (c), and TFC (d).

Cook, Cowper-Symonds and Ludwik were selected for the comparative numerical study.

Our simulation results and results obtained by other authors showed that constants of strain rate plasticity models reflect experimental results limited to the vicinity of specified points, but they may give significant local deviations along the entire strain rate, especially in the transition at the linear threshold of a strain rate. Classical rate-dependant plasticity models were fitted.

Considering the bilinear description of the yield strain-rate relationship, it was observed that the logarithmic Johnson-Cook plasticity model, with commonly used parameter values, adequately describes the low strain rate range. However, it deviates when exceeding the linear threshold. In the numerical simulation, it provides the 'softest' contact with the largest strain, the highest strain rate, and the lowest temperature of the particle after the impact. The power-law Cowper-Symonds model could be fitted to properly describe the high strain rate sensitivity range in the vicinity of the specified experimental points. However, it exhibits a large deviation of stresses in the range of strain rates around the linear threshold value and provides slightly higher stress at low strain rates. In the numerical simulation, the Cowper-Symonds model provides overall 'harder' contact that is characterised by the lowest strain and the highest particle temperature. The strain rate-independent Ludwik model, described by a single characteristic dynamic increase factor value, can also be used for dynamic problems. It gives an approximate resultant solution for the behaviour of a particle as a whole. Therefore, it is not suitable for evaluating microscopic parameters within the particle.

Generally, the quality of the elastic-plastic analysis depends on the adequacy of the plasticity model in describing a wide range of available experimental results. The case of the bilinear relationship between yield stress and strain rate makes it difficult to describe yielding by a single smooth function with fixed constants. Based on previous experimental results, a new two-function combined model, containing two independent expressions for each of the two ranges was proposed. The proposed model describes a low strain rate sensitivity range using the Johnson-Cook expression, and allows fitting of the model for experimental results in a high strain rate sensitivity range using a modified Cowper-Symonds expression.

Despite the drawbacks, the comparative FEM study of individual plasticity functions showed that they may be applied to illustrate the differences between 'hard' and 'soft' limits of experimentally obtained strain rate hardening results. These differences may be evaluated by comparing displacements, velocities, strains, strain rates, stresses, contact forces, temperatures, and their contribution to the material yield stress during the history of the impact.

Our results and comparison of available experimental results show that the issue of maximum strain rate remains still open. Maximum strain rates obtained by the comparative study show that local strain rates during impact exceed the strain rate limit of dislocation-based plasticity functions. Therefore, experimental evidence at the high strain rates is still necessary for the application of a continuum-based numerical FEM analysis. New problem-specific continuum models capable of describing both low and high strain-rate ranges could be elaborated using the impact-based experimental data. A more complex dislocation-based approach allows investigation of higher strain rates on a smaller scale related to crystal structure. However, the application of these methods to impact problem requires additional investigation on microscopic scale.

CRediT authorship contribution statement

Giedrius Jočbalis: Investigation, Validation, Software, Writing – original draft. **Rimantas Kačianauskas:** Conceptualization, Supervision, Writing – review & editing, Project administration. **Sergėjus Borodinas:** Visualization, Funding acquisition, Software. **Jerzy Rojek:** Resources, Methodology, Validation.

Declaration of Competing Interest

The authors declare that they have no known competing financial interests or personal relationships that could have appeared to influence the work reported in this paper.

Data Availability

Data will be made available on request.

Supplementary materials

Supplementary material associated with this article can be found, in the online version, at doi:10.1016/j.ijimpeng.2022.104394.

References

[1] Moridi A, Hassani-Gangaraj SM, Guagliano M, Dao M. Cold spray coating: review of material systems and future perspectives. Surf Eng 2014;30:369–95. https://doi.org/10.1179/1743294414Y.0000000270.

[2] Dowding I, Hassani M, Sun Y, Veysset D, Nelson KA, Schuh CA. Particle size effects in metallic microparticle impact-bonding. Acta Mater 2020;194:40–8. https://doi.org/10.1016/j.actamat.2020.04.044.

[3] Kuroda S, Watanabe M, Kim K, Katanoda H. Current status and future prospects of warm spray technology. J Therm Spray Technol 2011;20:653–76. https://doi.org/10.1007/s11666-011-9648-7.

[4] Oviedo F, Valarezo A. Residual stress in high-velocity impact coatings: parametric finite element analysis approach. J Therm Spray Technol 2020;29:1268–88. https://doi.org/10.1007/s11666-020-01026-5.

[5] Ludwik P. Elemente der technologischen mechanik. Berlin Heidelberg: Springer; 1909.

[6] Hollomon JH. Tensile deformation. Met Technol 1945;12:268–90.

[7] Swift HW. Plastic instability under plane stress. J Mech Phys Solids 1952;1:1–18. https://doi.org/10.1016/0022-5096(52)90002-1.

[8] Voce E. The relationship between stress and strain for homogeneous deformations, 1948.

[9] Ghaednia H, Wang X, Saha S, Xu Y, Sharma A, Jackson RL. A review of elastic–plastic contact mechanics. ASME Appl Mech Rev 2017;69:060804 1–30. https://doi.org/10.1115/1.4038187.

[10] Cundall PA, Strack ODL. A discrete numerical model for granular assemblies. Geotechnique 1979;29:47–65.

[11] Johnson KL. Contact mechanics. 1st ed. Cambridge: Cambridge University Press; 1987.

[12] Thornton C. Coefficient of restitution for collinear collisions of elastic-perfectly plastic spheres. J Appl Mech 1997;64:383–6. https://doi.org/10.1115/1.2787319.

[13] Zhang X, Vu-Quoc L. Modeling the dependence of the coefficient of restitution on the impact velocity in elasto-plastic collisions. Int J Impact Eng 2002;27:317–41. https://doi.org/10.1016/S0734-743X(01)00052-5.

[14] Weir G, Tallon S. The coefficient of restitution for normal incident, low velocity particle impacts. Chem Eng Sci 2005;60:3637–47. https://doi.org/10.1016/j.ces.2005.01.040.

[15] Rojek J, Lumelskyj D, Nosewicz S, Romelczyk-Baishya B. Numerical and experimental investigation of an elastoplastic contact model for spherical discrete elements. Comput Part Mech 2019;6:383–92. https://doi.org/10.1007/s40571-018-00219-8.

[16] Minamoto H, Kawamura S. Effects of material strain rate sensitivity in low speed impact between two identical spheres. Int J Impact Eng 2009;36:680–6. https://doi.org/10.1016/j.ijimpeng.2008.10.001.

[17] Hor A, Morel F, Lou Lebrun J, Germain G. Modelling, identification and application of phenomenological constitutive laws over a large strain rate and temperature range. Mech Mater 2013;64:91–110. https://doi.org/10.1016/j.mechmat.2013.05.002.

[18] Raletz F, Vardelle M, Ezo'o G. Critical particle velocity under cold spray conditions. Surf Coat Technol 2006;201:1942–7. https://doi.org/10.1016/j.surfcoat.2006.04.061.

[19] Price MC, Kearsley AT, Burchell MJ. Validation of the Preston–Tonks–Wallace strength model at strain rates approaching ~10^11 s^−1 for Al-1100, tantalum and copper using hypervelocity impact crater morphologies. Int J Impact Eng 2013;52: 1–10. https://doi.org/10.1016/j.ijimpeng.2012.09.001.

[20] Johnson GR, Cook WH. Fracture characteristics of three metals subjected to various strains, strain rates, temperatures and pressures. Eng Fract Mech 1985;21:31–48. https://doi.org/10.1016/0013-7944(85)90052-9.

[21] Sokolovskii VV. Propagation of elastic-viscoplastic waves in bars. Prikl Mat Mekh 1948;12:261–80.

[22] Cowper G., Symonds P. Technical report (Brown University. Division of Applied Mathematics), Strain-hardening and strain-rate effects in the impact loading of cantilever beams. 1957. 10.21236/AD0144762.

[23] Huh H, Kang WJ. Crash-worthiness assessment of thin-walled structures with the high-strength steel sheet. Int J Veh Des 2002;30:1–21. https://doi.org/10.1504/IJVD.2002.002022.

[24] Tuazon BJ, Bae K-O, Lee S-H, Shin H-S. Integration of a new data acquisition/processing scheme in SHPB test and characterization of the dynamic material properties of high-strength steels using the optional form of Johnson-Cook model. J Mech Sci Technol 2014;28:3561–8. https://doi.org/10.1007/s12206-014-0817-8.

[25] Couque H. The use of the direct impact Hopkinson pressure bar technique to describe thermally activated and viscous regimes of metallic materials. Phil Trans R Soc A 2014;372:1–10. https://doi.org/10.1098/rsta.2013.0218.

[26] Yu SS, Bin Lu Y, Cai Y. The strain-rate effect of engineering materials and its unified model. Lat Am J Solids Struct 2013;10:833–44. https://doi.org/10.1590/s1679-78252013000400010.

[27] Zhao H, Gary G. The testing and behaviour modelling of sheet metals at strain rates from 10−4 to 104 s−1. Mater Sci Eng A 1996;207:46–50. https://doi.org/10.1016/0921-5093(95)10017-2.

[28] Vinh A., Afzali T., Roche M. Mechanical behavior of materials. New York: K.J. Miller, R.F. Smith. Press, Oxford; 1980.

[29] Wu C, Li L, Thornton C. Rebound behaviour of spheres for plastic impacts. Int J Impact Eng 2003;28:929–46. https://doi.org/10.1016/S0734-743X(03)00014-9.

[30] Schmidt T, Assadi H, Gärtner F, Richter H, Stoltenhoff T, Kreye H, et al. From particle acceleration to impact and bonding in cold spraying. J Therm Spray Technol 2009;18:794–808. https://doi.org/10.1007/s11666-009-9357-7.

[31] Yokoyama K, Watanabe M, Kuroda S, Gotoh Y, Schmidt T, Gärtner F. Simulation of solid particle impact behavior for spray processes. Mater Trans 2006; 47:1697–702. https://doi.org/10.2320/matertrans.47.1697.

[32] Mebdoua Y, Fizi Y, Bouhelal N. Cold sprayed copper coating: numerical study of particle impact and coating characterization. Eur Phys J Appl Phys 2016;74. https://doi.org/10.1051/epjap/2015150316.

[33] Li G, Wang X, Li W. Effect of different incidence angles on bonding performance in cold spraying. Trans Nonferr Metals Soc China 2007;17:116–21. https://doi.org/10.1016/S1003-6326(07)60058-2.

[34] Razavipour M, Jodoin B. Material model for predicting dynamic response of copper and nickel at very high strain rates under cold spray conditions. J Therm Spray Technol 2021. https://doi.org/10.1007/s11666-020-01137-z.

[35] Petkevič R, Jočbalis G, Steponavičiūtė A, Stravinskas K, Romanov A, Kačianauskas R, et al. Numerical study of powder flow nozzle for laser-assisted metal deposition. Mathematics 2021;9:2913. https://doi.org/10.3390/math9222913.

[36] Xie W, Alizadeh-Dehkharghani A, Chen Q, Champagne VK, Wang X, Nardi AT, et al. Dynamics and extreme plasticity of metallic microparticles in supersonic collisions /639/166/988 /639/301/1023/1026 /639/301/930/12 /128 article. Sci Rep 2017;7:1–9. https://doi.org/10.1038/s41598-017-05104-7.

[37] Tu F, Delbergue D, Miao H, Klotz T, Brochu M, Bocher P, et al. A sequential DEM-FEM coupling method for shot peening simulation. Surf Coat Technol 2017;319: 200–12. https://doi.org/10.1016/j.surfcoat.2017.03.035.

[38] Zhang W, Liu K, Zhou J, Chen R, Zhang N, Lian G. Characteristic analysis of the stress propagation of metal powder in high velocity compaction using DEM. J Phys Soc Jpn 2020;89:044602. https://doi.org/10.7566/JPSJ.89.044602.

[39] Armstrong RW, Elban WL, Walley SM. Elastic, plastic, cracking aspects of the hardness of materials. Int J Mod Phys B 2013;27:1330004 1–79. https://doi.org/10.1142/S0217979213300041.

[40] Lea LJ, Jardine AP. Characterisation of high rate plasticity in the uniaxial deformation of high purity copper at elevated temperatures. Int J Plast 2018;102: 41–52. https://doi.org/10.1016/j.ijplas.2017.11.006.

[41] Lea L, Brown L, Jardine A. Time limited self-organized criticality in the high rate deformation of face centered cubic metals. Commun Mater 2020;1. https://doi.org/10.1038/s43246-020-00090-2.

[42] Fan H, Wang Q, El-Awady JA, Raabe D, Zaiser M. Strain rate dependency of dislocation plasticity. Nat Commun 2021;12:1–11. https://doi.org/10.1038/s41467-021-21939-1.

[43] Al Salahi AA, Othman R. Constitutive equations of yield stress sensitivity to strain rate of metals: a comparative study. J Eng 2016:3279047 1–7. https://doi.org/10.1155/2016/3279047. 2016.

[44] Rusinek A, Rodríguez-Martínez JA, Arias A. A thermo-viscoplastic constitutive model for FCC metals with application to OFHC copper. Int J Mech Sci 2010;52: 120–35. https://doi.org/10.1016/j.ijmecsci.2009.07.001.

[45] Almasri AH, Voyiadjis GZ. Effect of strain rate on the dynamic hardness in metals. J Eng Mater Technol Trans ASME 2007;129:505–12. https://doi.org/10.1115/1.2744430.

[46] Follansbee PS, Kocks UF. A constitutive description of the deformation of copper based on the use of the mechanical threshold stress as an internal state variable. Acta Metall 1988;36:81–93. https://doi.org/10.1016/0001-6160(88)90030-2.

[47] Field JE, Dear JP, Ogren JE. The effects of target compliance on liquid drop impact. J Appl Phys 1989;65:533–40. https://doi.org/10.1063/1.343136.

[48] Quinney H, Taylor GI. The emission of the latent energy due to previous cold working when a metal is heated. Proc R Soc Lond Ser A 1937;163:157–81. https://doi.org/10.1098/rspa.1937.0217.

[49] Kositski R, Mordehai D. Employing molecular dynamics to shed light on the microstructural origins of the Taylor-Quinney coefficient. Acta Mater 2021;205: 116511. https://doi.org/10.1016/j.actamat.2020.116511.

[50] Champagne VK, Helfritch DJ, Trexler MD, Gabriel BM. The effect of cold spray impact velocity on deposit hardness. Model Simul Mater Sci Eng 2010;18:065011. https://doi.org/10.1088/0965-0393/18/6/065011.

[51] Schmidt T, Gärtner F, Assadi H, Kreye H. Development of a generalized parameter window for cold spray deposition. Acta Mater 2006;54:729–42. https://doi.org/10.1016/j.actamat.2005.10.005.

[52] Rahmati S, Jodoin B. Physically based finite element modeling method to predict metallic bonding in cold spray. J Therm Spray Technol 2020;29:611–29. https://doi.org/10.1007/s11666-020-01000-1.

[53] Contact Analysis Theory n.d. https://doc.comsol.com/5.5/doc/com.comsol.help.sme/sme_ug_theory.06.65.html (accessed March 1, 2022).

[54] Low-Reflecting Boundary Condition n.d. https://doc.comsol.com/5.5/doc/com.comsol.help.sme/sme_ug_theory.06.57.html (accessed January 5, 2022).

[55] Kumar JP. Effect of temperature distribution in ultrasonically welded joints of copper wire and sheet used for electrical contacts. Materials (Basel) 2018;11(6): 1010 1–13. https://doi.org/10.3390/ma11061010.

[56] COMSOL Multiphysics® n.d.

[57] Xie J., Nelias D., Ogawa K., Ichikawa Y. Simulation of the Cold Spray Particle Deposition Process 2015. 10.1115/1.4030257.

[58] Coefficient of Friction Equation and Table Chart - Engineers Edge n.d. https://www.engineersedge.com/coeffients_of_friction.htm (accessed January 25, 2022).

[59] Ledbetter HM, Naimon ER. Elastic properties of metals and alloys. II. Copper. J Phys Chem Ref Data 1974;3:897–935. https://doi.org/10.1063/1.3253150.

[60] Tabor D. The hardness of metals. New York: Oxford university press; 1951.

[61] Etsion I, Kligerman Y, Kadin Y. Unloading of an elastic–plastic loaded spherical contact. Int J Solids Struct 2005;42:3716–29. https://doi.org/10.1016/j.ijsolstr.2004.12.006.

[62] Meyers MA, Gregori F, Kad BKK, Schneider MSS, Kalantar DHH, Remington BAA, et al. Laser-induced shock compression of monocrystalline copper: characterization and analysis. Acta Mater 2003;51:1211–28. https://doi.org/10.1016/S1359-6454(02)00420-2.

[63] Murphy WJ, Higginbotham A, Kimminau G, Barbrel B, Bringa EM, Hawreliak J, et al. The strength of single crystal copper under uniaxial shock compression at 100GPa. J Phys.: Condens Matter 2010;22(6). https://doi.org/10.1088/0953-8984/22/6/065404.

[64] Tong W, Clifton RJ, Huang S. Pressure-shear impact investigation of strain rate history effects in oxygen-free high-conductivity copper. J Mech Phys Solids 1992; 40:1251–94. https://doi.org/10.1016/0022-5096(92)90015-T.

[65] Hassani M, Veysset D, Nelson KA, Schuh CA. Material hardness at strain rates beyond 106 s−1 via high velocity microparticle impact indentation. Scr Mater 2020;177:198–202. https://doi.org/10.1016/j.scriptamat.2019.10.032.

[66] Bringa EM, Rosolankova K, Rudd RE, Remington BA, Wark JS, Duchaineau M, et al. Shock deformation of face-centred-cubic metals on subnanosecond timescales. Nat Mater 2006;5:805–9. https://doi.org/10.1038/nmat1735.

[67] Zhong WZ, Rusinek A, Jankowiak T, Abed F, Bernier R, Sutter G. Influence of interfacial friction and specimen configuration in Split Hopkinson Pressure Bar system. Tribol Int 2015;90:1–14. https://doi.org/10.1016/j.triboint.2015.04.002.